Intrinsic Berry curvature driven anomalous Nernst thermopower in the semimetallic Heusler alloy CoFeVSb

Amit Chanda, Jadupati Nag, Aftab Alam, K. G. Suresh, Manh-Huong Phan, and Hariharan Srikanth

Phys. Rev. B **107**, L220403 — Published 16 June 2023

DOI: 10.1103/PhysRevB.107.L220403

Intrinsic Berry curvature driven anomalous Nernst thermopower in the semi-metallic Heusler alloy CoFeVSb

Amit Chanda[1*], Jadupati Nag[2], Aftab Alam[2], K. G. Suresh[2*], Manh-Huong Phan[1] and Hariharan Srikanth[1*]

[1]*Department of Physics, University of South Florida, Tampa FL 33620*

[2]*Department of Physics, Indian Institute of Technology Bombay, Mumbai - 400076, India*

**Corresponding authors: achanda@usf.edu; suresh@phy.iitb.ac.in; sharihar@usf.edu*

Abstract

Understanding of spin-heat coupling mechanisms and magneto-thermoelectric phenomena, including the anomalous Nernst effect (ANE), in emergent quaternary Heusler alloys is of practical importance for applications in thermal management and energy harvesting. Here, we demonstrate an intrinsic Berry curvature mediated anomalous Nernst thermopower in CoFeVSb, which orders magnetically at high temperature ($T_C \approx 850$ K) with a large saturation magnetization of $\approx 2.2\ \mu_B/\mathrm{f.u.}$ at room temperature. We show that the electron-electron elastic and electron-magnon inelastic scattering dominate longitudinal electrical transport at low temperatures ($T \leq 50\ \mathrm{K}$), whereas the electron-phonon and electron-magnon scatterings govern it at higher T. The longitudinal thermopower is resulted mainly from the diffusive contribution, with a very large longitudinal Seebeck coefficient ($\approx 42\ \mu\mathrm{V.K^{-1}}$ at 395 K). The value of the anomalous Nernst coefficient (S_{ANE}) for CoFeVSb at room temperature is $\approx 0.039\ \mu\mathrm{V.K^{-1}}$ which is higher than the compressively strained $SrRuO_3$ film ($0.03\ \mu\mathrm{V.K^{-1}}$) as well as the spin gapless semiconductor CoFeCrGa ($0.018\ \mu\mathrm{V.K^{-1}}$). On lowering T, both the ordinary Nernst coefficient and carrier mobility increase but an opposite trend is found for S_{ANE}. Our ab-initio simulations reveal the topological semimetallic nature of CoFeVSb with a pair of Weyl points. These Weyl crossings result in a significant contribution to the Berry curvature, leading to an intrinsic anomalous Hall conductivity (σ_{xy}^{AHE}) of ≈ 85 S/cm, which matches well with experiment (77 S/cm at 2 K). Our experimental findings and *ab-initio* calculations support the dominance of the intrinsic Berry curvature in the observed ANE. The ratio of σ_{xy}^{AHE} to the transverse anomalous thermoelectric conductivity (α_{xy}^{ANE}) shows an increasing trend with T attaining a sizable fraction of $\frac{k_B}{e}$ $\left(\approx 0.35\frac{k_B}{e}\right)$ at room temperature.

Keywords: Heusler alloys, transverse thermoelectricity, anomalous Nernst effect, thermoelectric conductivity, Berry curvature

I. INTRODUCTION

Current advancement in the field of spin-heat coupling [1–4] and transport of thermally generated charge carriers has revived the interest in transverse magneto-thermoelectric phenomena, *e.g.*, the anomalous Nernst effect (ANE) [5], the anomalous Ettingshausen effect (AEE), [6] *etc*. The ANE is the thermal analog of the anomalous Hall effect (AHE), and described as a magneto-thermoelectric phenomenon wherein an electric field is generated by applying a thermal gradient and a transverse magnetic field to a magnetic conductor/semiconductor [5,7]. Because of the large Berry curvature near the Fermi level, topological ferromagnets Co_2MnGa [8,9], $Co_3Sn_2S_2$ [10,11], Fe_3Ga [12], Fe_3Sn [13] *etc*., exhibit very large anomalous Nernst conductivity within the range $0.5-5\ \mathrm{A\cdot m^{-1}\cdot K^{-1}}$. Very recently, the non-centrosymmetric Kagome ferromagnet $UCo_{0.8}Ru_{0.2}Al$ [14] and the noncollinear topological antiferromagnet $YbMnBi_2$ [15] have been reported to show colossal anomalous Nernst conductivities of $15\ \mathrm{A\cdot m^{-1}\cdot K^{-1}}$ and $10\ \mathrm{A\cdot m^{-1}\cdot K^{-1}}$, respectively at low temperatures. While the intrinsic Berry curvature driven large ANEs have been reported in some Heusler alloys based topological ferromagnets [8,9,16], other Heusler ferromagnets exhibit an extrinsic skew scattering dominated ANE [17–19].

Among the Heusler systems of current interest, CoFeVSb possesses a very high ordering temperature ($T_C \approx 850\mathrm{K}$) and a large saturation magnetization of $\approx 2.2\ \mu_\mathrm{B}/\mathrm{f.u.}$at room temperature [20]. This quaternary Heusler alloy shows asymmetric magnetoresistance (MR) at room temperature, indicative of the spin-valve like nature of the material in its bulk form [20]. *Ab initio* calculations have shown that this system is composed of energetically competing ferromagnetic(FM)/antiferromagnetic(AFM) interface structures embedded in an FM matrix, which gives rise to the spin valve-like MR feature [20]. The AHE has also been observed in this system over a broad temperature range ($4\mathrm{K} \leq T \leq 395\mathrm{K}$) and attributed to the dominating intrinsic Berry phase contribution. Furthermore, this sample possesses a very high value of thermoelectric power factor $\approx 0.62\mathrm{mW.\,m^{-1}.\,K^{-2}}$ at room temperature, making it a promising thermoelectric material. The coexistence of these striking physical properties in a single phase of CoFeVSb prompted us to investigate its spin-caloritronic properties. Here, we report on a comprehensive investigation of electrical, thermal, and magnetothermoelectric properties with an emphasis on the ANE in CoFeVSb.

II. EXPERIMENTAL DETAILS

Polycrystalline sample of CoFeVSb were synthesized by arc melting technique. The synthesis method and the crystal-phase characterization of the sample have been reported elsewhere [20]. The static magnetic properties of the sample were characterized using a vibrating sample magnetometer (VSM) attachment with a physical property measurement system (PPMS), Quantum Design. The longitudinal electrical resistivity (ρ_{xx}), longitudinal thermopower (S_{xx}), and thermal conductivity (κ_{xx}) were simultaneously measured with the Thermal Transport Option (TTO) of the PPMS. A sample with dimensions $5 \times 4 \times 1\ \mathrm{mm}^3$ was used for Hall/Nernst measurements. A standard four-probe technique was employed for the Hall measurements. A DC current, I_{DC}=8mA was sourced through the current leads using a Keithley 2400 source-meter and the average Hall voltage was recorded as, $V_H = \frac{[V(+I)-V(-I)]}{2}$ using a Keithley 2182A nanovoltmeter. The background-corrected Hall voltage was estimated as, $V_{xy}^{Hall} = \frac{[V_H(+H_{max})-V_H(-H_{max})]}{2}$, where, H_{max} is the maximum value of applied magnetic field. The Hall resistivity was estimated as $\rho_{xy} = \frac{V_{xy}^{Hall} L_Z}{I_{DC}}$, where, L_Z = sample thickness. The Nernst measurements on the CoFeVSb sample were performed by employing a home-built spin-caloritronic measurement set up integrated with the PPMS. A detailed description of our experimental set up is reported elsewhere [17] and in the Supplemental Material (SM) [21].

III. RESULTS AND DISCUSSION

The main panel of **Fig. 1**(a) demonstrates the temperature (T)-dependence of ρ_{xx} for CoFeVSb in the range: 4K $\leq T \leq$ 395K. Evidently, $\rho_{xx}(T)$ exhibits metallic-like resistivity $\left(\frac{\partial \rho_{xx}}{\partial T} > 0\right)$ throughout the T-range along with a slope-change below 50K (see inset of **Fig. 1**(a)). The $\rho_{xx}(T)$ data for CoFeVSb was found to fit well with the expression: $\rho_{xx}(T) = \rho_0 + A.\left(\frac{T}{\theta_D}\right)^5 \int_0^{\frac{\theta_D}{T}} \frac{e^x x^5 dx}{(e^x-1)^2} + C.T^2 e^{-(T/\Delta)}$ in the high-T region (above 50K), where, ρ_0 represents the T-independent residual resistivity, the second-term represents the electron-phonon scattering contribution according to the Bloch-Grüneisen model (A = constant pre-factor and θ_D =Debye temperature) [22–24] and, the third-term signifies the contribution from electron-magnon scattering (C = constant pre-factor, $k_B\Delta$ is the spin wave energy gap which represents the difference between the Fermi level and the nearest band edge of unoccupied minority spins [24], and k_B is the Boltzmann constant). In the case of half-metals, the T^2-dependent electron-magnon scattering contribution is exponentially suppressed due to the gapped spin-flip scattering [24–26]. We fitted the $\rho_{xx}(T)$ curve with the expression: $\rho_{xx}(T) = \rho_0 + \rho_{elastic}T^{1/2} + C.T^2 e^{-(T/\Delta)}$ in the low-T region (below 50K) region [26], where the second-term accounts for the electron-electron elastic scattering contribution with a $T^{1/2}$-dependence at low-T [27]. From the high-T fit, we obtained $\rho_0 = (1.3 \pm 0.01) \times 10^{-4}\ \Omega.\mathrm{cm}$, $A = (2.04 \pm 0.06) \times 10^{-4}\ \Omega.\mathrm{cm.K^{-5}}$, $C = (5.07 \pm 0.2) \times 10^{-11}\ \Omega.\mathrm{cm.K^{-2}}$, $\theta_D = (313 \pm 2)$ K and $\Delta = (40 \pm 5)$ K. The fitting parameters extracted from the low-T fit are $\rho_0 = (1.2 \pm 0.02) \times 10^{-4}\ \Omega.\mathrm{cm}$, $\rho_{elastic} = (-3.34 \pm 0.1) \times 10^{-7}\ \Omega.\mathrm{cm}\ .\ \mathrm{K^{-1/2}}$, $C = (2.7 \pm 0.1) \times 10^{-9}\ \Omega.\mathrm{cm.K^{-2}}$ and $\Delta = (40 \pm 3)$ K.

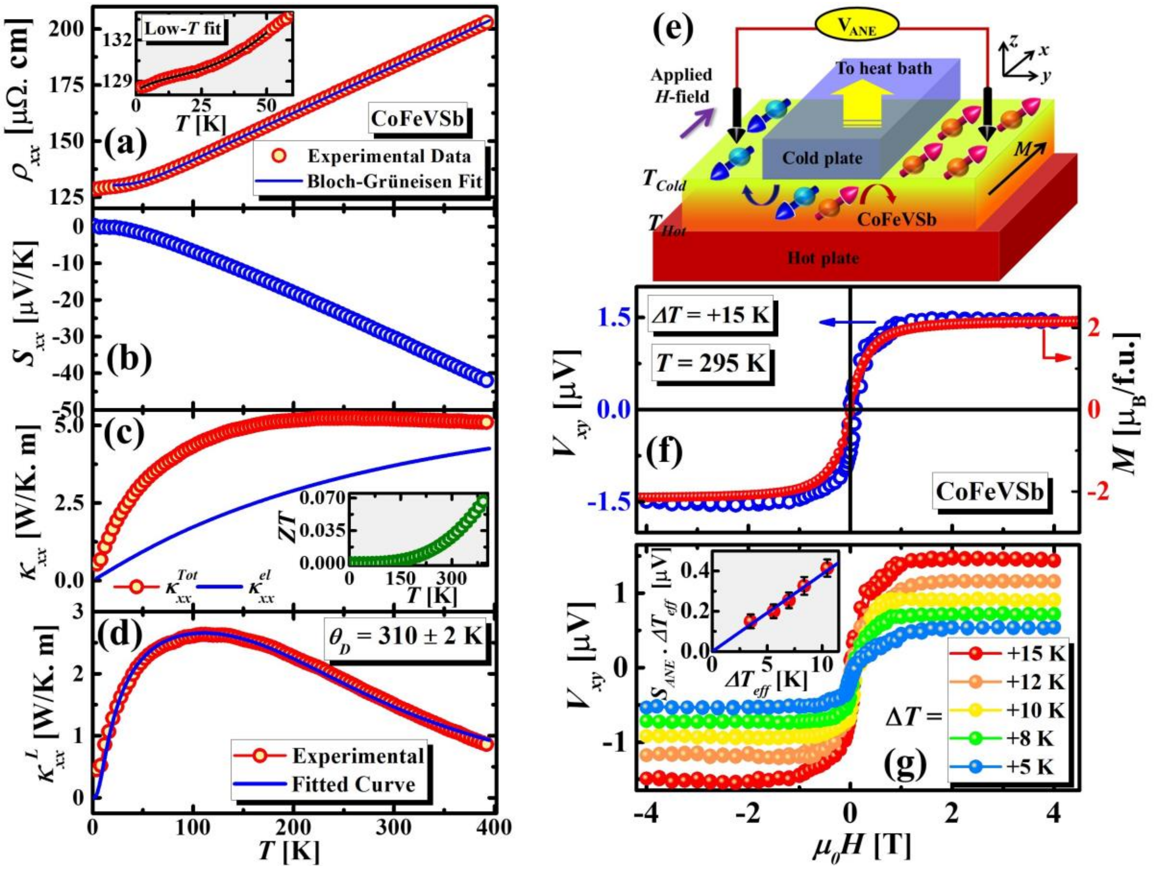

FIG. 1(a) Main panel: T-dependence of ρ_{xx} of CoFeVSb, fitted with $\rho_{xx}(T) = \rho_0 + A.\left(\frac{T}{\theta_D}\right)^5 \int_0^{\frac{\theta_D}{T}} \frac{e^x x^5 dx}{(e^x-1)^2} + C.T^2 e^{-(T/\Delta)}$in the high-$T$ region and inset: fitting with $\rho_{xx}(T) = \rho_0 + \rho_{elastic} T^{1/2} + C.T^2 e^{-(T/\Delta)}$in the low-$T$ region. (b) T-dependence of S_{xx}. (c) Main panel: T-dependence of κ_{xx}^{Tot} and κ_{xx}^{el}, inset: T-dependence of thermoelectric figure of merit, ZT. (d) T-dependence of κ_{xx}^{L} fitted with Callaway's model. (e) Schematic illustration of Nernst measurement. (f) Left y-scale: H-dependence of the Nernst voltage, $V_{xy}(H)$ for $\Delta T = +15$K and right y-scale: $M(H)$ at 295K. (g) Main panel: $V_{xy}(H)$ for different values of ΔT at 295K, inset: background corrected anomalous Nernst voltage, $S_{ANE} \times \Delta T_{eff}$ as a function of ΔT_{eff}.

The values of Δ obtained from the fits for CoFeVSb are close to that reported for the well-known half-metallic CrO_2 ($\Delta \approx$ 80K), [25] Fe_2Si ($\Delta \approx$ 85K), [26] and Co_2FeSi ($\Delta \approx$100K), [24] which strongly indicates the half-metallic nature of this sample. **Fig. 1**(b) represents the T-dependence of S_{xx} for CoFeVSb. The sign of $S_{xx}(T)$ is negative throughout the measured T-range, indicating electrons as the dominant carrier for the thermally-driven charge-transport. Moreover, $|S_{xx}|$ decreases linearly from ≈ 42μV.K^{-1} at 395K and approaches zero at low-*T* indicating the dominant contribution of the diffusive component of thermopower [28].

As shown in the main panel of **Fig. 1**(c), the total longitudinal thermal conductivity, $\kappa_{xx}^{Tot}(T)$ remains almost unchanged in the *T*-range: $200\text{K} \leq T \leq 395\text{K}$, but decreases slowly below 200K and rapidly below 100K. The *T*-dependence of the electronic thermal conductivity, $\kappa_{xx}^{el}(T)$ is usually estimated from the Wiedemann Franz law: $\kappa_{xx}^{el} = \frac{L_0 T}{\rho_{xx}}$, where, $L_0 = \frac{\pi^2 k_B^2}{3e^2} = 2.44 \times 10^{-8}\ \text{W.}\Omega\text{.K}^{-1}$ is the Lorenz number for free electrons (degenerate-limit) [29]. However, L_0 was shown to deviate from the degenerate-limit for semiconductors with large value of S_{xx}. [30] To account for this discrepancy, L_0 for such semiconductors was proposed to be accurately estimated using the expression, $L_0 = 1.5 + \exp\left(-\frac{|S_{xx}|}{116}\right)$. [30] Since $|S_{xx}|$ for our sample is very high at high-*T*, we estimated $\kappa_{xx}^{el}(T)$ using the expression, [30] $\kappa_{xx}^{el}(T) = \frac{\left[1.5+\exp\left(-\frac{|S_{xx}|}{116}\right)\right]T}{\rho_{xx}}$, as shown in the main panel of **Fig. 1**(c). The main panel of **Fig. 1**(d) shows the *T*-dependence of the lattice thermal conductivity, $\kappa_{xx}^{L}(T)$ obtained from the expression: $\kappa_{xx}^{L}(T) = [\kappa_{xx}^{Tot}(T) - \kappa_{xx}^{el}(T)]$. Evidently, $\kappa_{xx}^{L}(T)$ increases considerably with decreasing temperature down to 100K at which it shows a broad maximum and then decreases rapidly with further lowering of the temperature. As shown in the main panel of **Fig. 1**(d), we fitted $\kappa_{xx}^{L}(T)$ for CoFeVSb with the Debye-Callaway model, [31,32]

$$\kappa_{xx}^{L}(T) = \frac{k_B}{2\pi^2 v_S}\left(\frac{2\pi k_B T}{h}\right)^3 \int_0^{\left(\theta_D/T\right)} \frac{\tau_L z^4 e^z}{(e^z-1)^2}\, dz \qquad (1)$$

Here, v_S is the average phonon velocity (approximately equals to the sound velocity), $z = \frac{\hbar\omega}{k_B T}$, $\omega =$ phonon frequency, and τ_L = total phonon relaxation-time. The values of the fitting parameters *A*, *B*, *C* and θ_D are (9.95 ± 2) x 10^{-42} s^3, (7.45 ± 3) x 10^{-23} s. K^{-1}, (4.5 ± 1) x 10^{-18} s and (310 ± 5) K, respectively. The thermoelectric figure of merit, $ZT = \frac{S_{xx}^2}{\kappa_{xx}^{Tot}\rho_{xx}}T$ [33] for CoFeVSb (inset of **Fig. 1**(c)) is ≈ 0.07 at 395K which decreases gradually with decreasing temperature.

The schematic illustration of our transverse thermoelectric transport measurement is shown in **Fig. 1**(e). The DC magnetic field (H) is applied along the x-axis and the T-gradient is along the sample thickness (z-axis). The Nernst voltage generated along the y-axis was measured using a Keithley 2182A nanovoltmeter while sweeping H. The left y-scale of **Fig. 1**(f) exhibits the H-dependence of the Nernst voltage, $V_{xy}(H)$ for a fixed value of the T-difference between the top plate (T_{hot}) and the bottom plate (T_{cold}; $T_{hot} > T_{cold}$), $\Delta T = (T_{hot} - T_{cold}) = +15$K for the CoFeVSb sample at $T = \frac{T_{hot}+T_{cold}}{2}$ = 295K. The right y-scale of **Fig. 1**(f) shows the isothermal magnetization, $M(H)$ at 295K. Clearly, the $V_{xy}(H)$ loop shows negligible hysteresis and replicates the corresponding $M(H)$ behavior. Since the thermally generated electric field induced by ANE is proportional to the magnetization, *i.e.*, $\overrightarrow{\boldsymbol{E}_{ANE}} \propto \left(\mu_0 \overrightarrow{\boldsymbol{M}} \times \overrightarrow{\boldsymbol{\nabla T}}\right)$, [8,34] the observed feature of the $V_{xy}(H)$ loop originates from the ANE.

Note that the bulk thermal resistances of the sample and the N-grease layers as well as the interfacial thermal resistances cause drop in the actual T-gradient across the sample. [35] Ignoring the interfacial thermal resistances between the N-grease and the hot/cold plates as well as between the sample and N-grease layers, [17] the total T-difference between the hot and cold plates (ΔT) = effective T-difference across the sample (ΔT_{eff}) + drop in ΔT in the N-grease layers on both sides of the sample. Therefore, considering the 3-slab model, ΔT_{eff} can be expressed as, [17,36] $\Delta T_{eff} = \frac{\Delta T}{\left[1+\left(\frac{2d_{\text{N-Grease}}}{\kappa_{\text{N-Grease}}}\right)\left(\frac{\kappa_{\text{CoFeVSb}}}{d_{\text{CoFeVSb}}}\right)\right]}$, where, $d_{\text{N-Grease}}(d_{\text{CoFeVSb}})$ is the thickness of the grease-layer (CoFeVSb), $\kappa_{\text{N-Grease}}(\kappa_{\text{CoFeVSb}})$ is the thermal conductivity of the grease-layer (CoFeVSb), and A = cross-sectional area. Using the reported values of $\kappa_{\mathrm{N-Grease}}(T)$ of the N-grease, [37] , $d_{\mathrm{N-Grease}} \approx 10\mu\mathrm{m}$, $d_{\mathrm{CoFeVSb}} \approx 1\mathrm{mm}$, we estimated the T-dependence of ΔT_{eff} (see SM [21]).

In addition to the ANE contribution, the ordinary Nernst effect (ONE) also contributes to the total Nernst signal. The ONE contribution can be estimated from the slope of the slowly varying segment ($H_{sat} \leq H \leq H_{max}$) of the H-dependent transverse Seebeck coefficient, $S_{xy}(H)$ defined as, $S_{xy}(H) = \frac{V_{xy}(H)}{\Delta T_{eff}} \times \left(\frac{L_z}{L_y}\right)$. [34,38] Here, L_y(=3mm) is the distance between the voltage leads and $L_z(= 1\mathrm{mm})$ is the sample thickness. The ordinary Nernst coefficient (S_{ONE}) at 295K for CoFeVSb was estimated as $S_{ONE} = (-0.176 \pm 0.05)$ nV.K^{-1}.T^{-1}, which is smaller compared to other materials *e.g.*, Fe_3O_4 single crystal (S_{ONE} =10 nV.K^{-1}.T^{-1} at room temperature) [34]. The main panel of **Fig. 1**(g) demonstrates $V_{xy}(H)$ for different values of ΔT at 295K. Evidently, $V_{xy}(H)$ increases with ΔT. The inset of **Fig. 1**(g) shows the normalized anomalous Nernst voltage, $S_{ANE} \times \Delta T_{eff} = V_{ANE}(\mu_0 H_{max}) \times \left(\frac{L_z}{L_y}\right)$, as a function of ΔT_{eff} at 295K, where, S_{ANE} is the background-corrected anomalous Nernst coefficient, $V_{ANE}(\mu_0 H_{max})$ represents the background-corrected anomalous Nernst voltage defined as, $V_{ANE}(\mu_0 H_{max}) = \left[\frac{V_{xy}(+\mu_0 H_{max}) - V_{xy}(-\mu_0 H_{max})}{2}\right]$ and $\mu_0 H_{max}$ = maximum applied magnetic field ($\mu_0 H_{max} \gg \mu_0 H_{sat}$). Clearly, $\left(S_{ANE} \times \Delta T_{eff}\right)$ varies linearly with ΔT_{eff}.

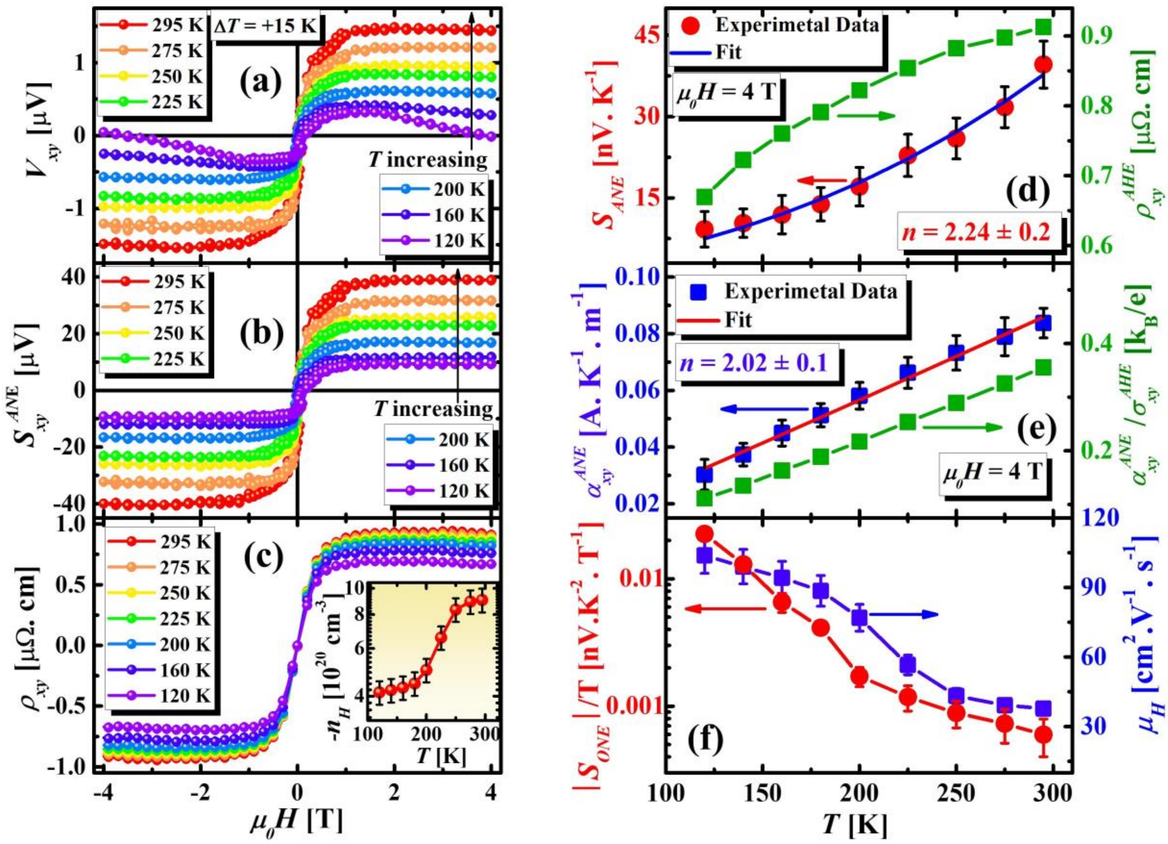

FIG. 2(a) $V_{xy}(H)$ for CoFeVSb at selected temperatures for ΔT = +15 K. (b) $S_{xy}^{ANE}(H)$ and (c) $\rho_{xy}(H)$ for CoFeVSb at selected temperatures. (d) Left *y*-scale: *T*-dependence of S_{ANE} fitted with Eqn. (2), and right *y*-scale: *T*-dependence of ρ_{xy}^{AHE}. (e) Left *y*-scale: *T*-dependence of α_{xy}^{ANE} fitted with Eqn. (3), and right *y*-scale: *T*-dependence of $\left(\alpha_{xy}^{ANE}/\sigma_{xy}^{AHE}\right)$. (f) Left *y*-scale: *T*-dependence of $(|S_{ONE}|/T)$, and right *y*-scale: *T*-dependence of μ_H.

Fig. 2(a) demonstrates the $V_{xy}(H)$ hysteresis loops for CoFeVSb at selected temperatures for ΔT = +15K. Notably, $|V_{xy}(H)|$ decreases with lowering temperature. Most importantly, $V_{xy}(H)$ shows prominent negative-slope in the high field region at low-*T*, and the absolute value of the slope increases drastically below 200K, indicating the enhanced ONE contribution at low-*T*. **Fig. 2**(b) shows the magnetic field dependence of the anomalous Nernst coefficient (ANC), $S_{xy}^{ANE}(H)$ at different temperatures, which was obtained by subtracting the ONE contribution from the total transverse Seebeck coefficient, $S_{xy}(H)$ as, $S_{xy}^{ANE}(H) = \left[S_{xy}(H) - S_{xy}^{ONE}(H)\right] = \left[S_{xy}(H) - |S_{ONE}|.H\right]$. Clearly, $|S_{xy}^{ANE}(H)|$ gradually decreases with decreasing-T. The left y-axis of **Fig. 2**(d) demonstrates the T-dependence of the background-corrected ANC, $S_{ANE}(\mu_0 H_{max}, T)$. At 295K, $|S_{ANE}| = 0.039$ μV.K^{-1} for CoFeVSb which is higher than the compressively-strained $SrRuO_3$ film (0.03 μV.K^{-1}) [39] as well as the spin-gapless semiconductor CoFeCrGa (0.018 μV.K^{-1}) [17].

Now, let us understand the origin of the non-linear T-dependence of $S_{ANE}(T)$ in CoFeVSb. The transverse thermoelectric coefficient (S_{xy}) is defined as, $S_{xy} = \left[\frac{\alpha_{xy} - S_{xx}\sigma_{xy}}{\sigma_{xx}}\right]$, where σ_{xy} and σ_{xx} are the transverse and longitudinal electrical conductivities which are expressed as, [5,9,40] $\sigma_{xy} = \left[\frac{-\rho_{xy}}{(\rho_{xx})^2 + (\rho_{xy})^2}\right]$ and $\sigma_{xx} = \left[\frac{\rho_{xx}}{(\rho_{xx})^2 + (\rho_{xy})^2}\right]$, respectively, and α_{xy} is the transverse thermoelectric conductivity [5,34]. According to the Mott's relations, $S_{xx} = \frac{\pi^2 k_B^2 T}{3e\sigma_{xx}}\left(\frac{\partial \sigma_{xx}}{\partial E}\right)_{E=E_F}$, and $\alpha_{xy} = \frac{\pi^2 k_B^2 T}{3e}\left(\frac{\partial \sigma_{xy}}{\partial E}\right)_{E=E_F}$, where e is the electronic charge and E_F is the Fermi energy. [5,41] It is known that the ANE and AHE share the common physical origin [5] Therefore, considering the power law for the AHE, $\rho_{xy}^{AHE} = \lambda M \rho_{xx}^{n}$, [5] where ρ_{xy}^{AHE} is the anomalous Hall resistivity, ρ_{xx} is the longitudinal resistivity, λ is the spin-orbit coupling constant and n is an exponent, the ANC can be expressed as, [5,34]

$$S_{xy}^{ANE} = \rho_{xx}^{n-1}\left[\frac{\pi^2 k_B^2 T}{3e}\left(\frac{\partial \lambda}{\partial E}\right)_{E=E_F} - (n-1)\lambda S_{xx}\right]. \qquad (2)$$

For $n = 1$, the extrinsic skew scattering is the leading mechanism for the anomalous Nernst/Hall transport, whereas for $n = 2$, the intrinsic Berry curvature becomes the dominating mechanism [42]. We fitted the $S_{ANE}(T)$ for CoFeVSb using **Eqn. 2** and the best fit was obtained for $n = 2.24 \pm 0.2$ which indicates that the origin of ANE in CoFeVSb is dominated by the intrinsic Berry curvature or, the side jump mechanism [42]. To confirm the origin of the observed ANE, we need to understand the temperature dependence of the anomalous off-diagonal thermoelectric conductivity, $\alpha_{xy}^{ANE}(T)$, which can be expressed as, [10,11,43]

$\alpha_{xy}^{ANE} = S_{xy}^{ANE}\sigma_{xx} + S_{xx}\sigma_{xy}^{AHE} = \left[\frac{S_{xy}^{ANE}\rho_{xx} - S_{xx}\rho_{xy}^{AHE}}{(\rho_{xx})^2 + \left(\rho_{xy}^{AHE}\right)^2}\right]$. Using the Mott's relations, α_{xy}^{ANE} can be written as, [5,34]

$$\alpha_{xy}^{ANE} = \rho_{xx}^{n-2}\left[\frac{\pi^2 k_B^2 T}{3e}\left(\frac{\partial\lambda}{\partial E}\right)_{E=E_F} - (n-2)\lambda S_{xx}\right] \tag{3}$$

The main panel of **Fig. 2**(c) illustrates the magnetic field dependence of Hall resistivity $\rho_{xy}(H)$ for CoFeVSb at few selected temperatures in the *T*-range: $120\text{K} \leq T \leq 295\text{K}$. Similar to the Nernst voltage, $\rho_{xy}(H)$ also shows the contributions from both ordinary Hall effect (OHE) and AHE along-with negative slope in the high field region throughout the temperature range, indicating electrons as the majority carriers. However, unlike the Nernst voltage, and the absolute value of the slope in $\rho_{xy}(H)$ increases slowly with decreasing temperature. Especially, at low-*T* (*e.g.*, 120K), the negative slope in the Nernst voltage is more robust compared to that in the Hall resistivity. Such striking difference in the Nernst and Hall signals has also been observed in the half-metallic semimetal $Co_3Sn_2S_2$. [11] From the slope of the slowly varying segment of $\rho_{xy}(H)$, we obtained the OHE contribution and estimated the *T*-dependence of the carrier-concentration, $n_H(T)$, as shown in the inset of **Fig. 2**(c). Clearly, $|n_H|$ decreases with decreasing temperature. By subtracting the OHE contribution from $\rho_{xy}(H)$, we evaluated the temperature dependence of anomalous Hall resistivity $\left(\rho_{xy}^{AHE}\right)$, as shown on the right-*y* scale of **Fig. 2**(d). [42] Similar to the ANC, ρ_{xy}^{AHE} also decreases with decreasing temperature. Incorporating the *T*-dependences of S_{xx}, S_{ANE}, ρ_{xx} and ρ_{xy}^{AHE}, we evaluated the *T*-variation of α_{xy}^{ANE}, as shown on the left-*y* scale of **Fig. 2**(e). We fitted $\alpha_{xy}^{ANE}(T)$ for CoFeVSb using **Eqn. 3**, and the best fit was obtained for $n = 2.02 \pm 0.1$, which is close to that obtained from the $S_{ANE}(T)$ fit. This further confirms that both the ANE and AHE in CoFeVSb is governed by the intrinsic Berry curvature or, the side jump mechanism [42]. Notably, the ratio $\left[\left(\frac{\partial\lambda}{\partial E}\right)_{E=E_F}/\lambda\right]$ obtained from the $S_{ANE}(T)$ and $\alpha_{xy}^{ANE}(T)$ fits are 1.33×10^{19} and 2.04×10^{19}, respectively.

Next, we examine the correlation between the anomalous transverse thermoelectric conductivity $\left(\alpha_{xy}^{ANE}\right)$ and anomalous Hall conductivity $\left(\sigma_{xy}^{AHE}\right)$. While α_{xy}^{ANE} represents the transport of entropy, σ_{xy}^{ANE} determines the transport of charge-carriers and, $\left(\alpha_{xy}^{ANE}/\sigma_{xy}^{AHE}\right)$ should approach $\frac{k_B}{e}$ at high-*T* [14,44]. As shown on the left-*y* scale of **Fig. 2**(e), $\left|\alpha_{xy}^{ANE}/\sigma_{xy}^{AHE}\right|$ increases with increasing temperature and attains $\approx 0.35\frac{k_B}{e}$ at 295K, which is much lower than $UCo_{0.8}Ru_{0.2}Al$ $\left(\left|\alpha_{xy}^{ANE}/\sigma_{xy}^{AHE}\right| \approx 2\frac{k_B}{e} \text{ at } 47\text{K}\right)$ [14], but closer to that for Co_2MnGa, Mn_3Sn, $Co_3Sn_2S_2$ and $La_{0.7}Sr_{0.3}CoO_3$ [44]. Since the ordering temperature of CoFeVSb is very high $(T_C \approx 850\text{K})$ and, both $S_{ANE}(T)$ and $\left|\alpha_{xy}^{ANE}(T)/\sigma_{xy}^{AHE}(T)\right|$ for CoFeVSb are increasing with increasing temperature even at room temperature, it would be worth investigating high temperature ANE/AHE in this system to realize at what temperature(s) S_{ANE} shows a peak and $\left|\alpha_{xy}^{ANE}(T)/\sigma_{xy}^{AHE}(T)\right|$ approaches $\frac{k_B}{e}$. To confirm the origin of ANE in CoFeVSb, it is imperative to quantify the carrier mobility (μ_H). In semi-classical picture, $|S_{ONE}|$ scales linearly with μ_H through the expression, [11,45,46] $|S_{ONE}| = \frac{\pi^2}{3}\left(\frac{k_B}{e}\right)\left(\frac{k_B T}{E_F}\right)\mu_H$. However, $|S_{ANE}|$ is known to scale with $\left(\frac{1}{\mu_H}\right)$ if the origin of the ANE is dominated by the intrinsic Berry-curvature [11]. As shown in **Fig. 2**(f), both $(|S_{ONE}|/T)$ and μ_H increase with decreasing temperature. Furthermore, S_{ANE} decreases with decreasing temperature whereas μ_H shows the opposite *T*-dependence, which is in agreement with the intrinsic Berry-curvature picture of ANE [11].

We have further performed *ab-initio* band structure calculations to complement our experimental results. Computational details of these calculations are presented in reference [20] and SM [21]. **Figure 3**(a) shows the band structure revealing a pair of Weyl points above E_F (≈0.3eV) arising from the intersections of semi-metallic bands 28 and 29 (highlighted by red circles). The contribution to the density of states at/near E_F primarily arises from band numbers 27, 28 and 29 (see **Fig. 3**(b)). **Figure 3**(c) display the z-component of simulated Berry curvature ($-\Omega_z(k)$), along with its 2D projection in the k_z=0 and k_z=0.5 planes shown in **Figs. 3**(d)-(e). The spike in the Berry curvature along the L- Γ direction (see **Fig. 3**(c)) is due to two spin-semi metallic bands, 27 and 28 (see **Fig. 3**(a)). This spike arises from the small energy denominator in the Berry-curvature's definition along this *k*-path [42].

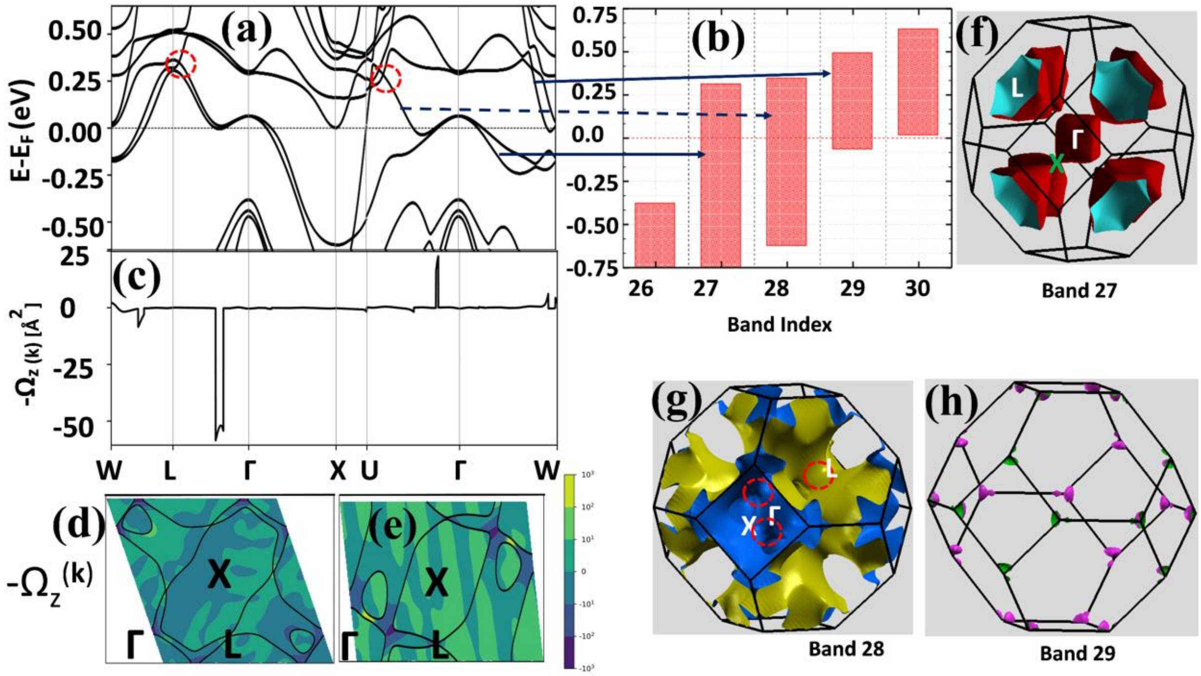

FIG. 3 For CoFeVSb, (a) Electronic band structure showing the topological non-trivial feature involving a pair of Weyl points at ≈ 0.3eV above E_F. (b) Widths of various semi metallic bands (27, 28, 29). (c) Calculated Berry curvature along the high symmetry path. (d)-(e) 2D projection of Berry curvature on k_z=0 and k_z=0.5 plane (f-h) Fermi surfaces originating from the semi metallic bands (27, 28, 29) indicating the location of electron/hole pockets and Weyl points.

A reasonably high intrinsic anomalous Hall-conductivity (AHC) value is obtained which is solely attributed to the large spike in $\Omega_z(k)$. The following equation was used to calculate AHC,

$$\sigma_{xy} = -\frac{e^2}{\hbar}\sum_p \int_{BZ} \frac{d^3k}{(2\pi)^3} f_p(k)\Omega_{p,z}(k) \qquad (4)$$

where $f_n(k)$ represents the Fermi-Dirac distribution function, $\Omega_{n,z}(k)$ is the z-component of the Berry curvature for n^{th} band, and the integration is over the entire Brillouin zone (BZ). The simulated value of intrinsic AHC is, σ^A_{int}= 85 S/cm, which matches well with the experimental value (77 S/cm at 2K). This implies that both intrinsic AHC and ANE mainly stem from the Berry curvature. We also simulated the Fermi surfaces related to the three semi-metallic bands (27, 28, and 29), as shown in **Figs. 3**(f)-(h). Two hole-pockets emerged along L-Γ points due to bands 27 and 28, while an electron-pocket appears from band 29. A pair of Weyl points is clearly visible in the Fermi surface, originating from band 28 (see **Fig. 3**(g)), as observed in the band structure along L-Γ, and U-Γ (see **Fig. 3**(a)), corroborating the topological non-trivial features of this alloy.

IV. CONCLUSIONS

In summary, we present a comprehensive study of the longitudinal and transverse thermoelectric properties with a special focus on the ANE in CoFeVSb. We have found that the anomalous Nernst coefficient (S_{ANE}) of CoFeVSb is $\approx 0.039\ \mu\mathrm{V.K}^{-1}$ at room temperature. Both ordinary Nernst coefficient (S_{ONE}) and carrier mobility (μ_H) increase upon lowering temperature, but an opposite trend is found for S_{ANE}. Our in-depth analysis confirmed that the observed ANE in this material is dominated by intrinsic Berry-curvature which is also supported by our *ab initio* calculations. Our band structure calculations confirm the topological non-trivial feature of CoFeVSb with a pair of Weyl points located slightly above E_F.

V. ACKNOWLEDGEMENTS

Financial support by the US Department of Energy, Office of Basic Energy Sciences, Division of Materials Science and Engineering under Award No. DE-FG02-07ER46438 is acknowledged. HS also thanks support from IIT Bombay for a short-term visiting professorship. KGS thanks DST/INT/TUS/RSF/P-47/2021 for the support via a sponsored project. AA acknowledges DST-SERB (Grant No. CRG/2019/002050) for funding to support this research.

REFERENCES

[1] K.-I. Uchida, *Transport Phenomena in Spin Caloritronics*, Proc. Japan Acad. Ser. B **97**, 69 (2021).

[2] G. E. W. Bauer, E. Saitoh, and B. J. Van Wees, *Spin Caloritronics*, Nat. Mater. **11**, 391 (2012).

[3] A. Chanda, C. Holzmann, N. Schulz, J. Seyd, M. Albrecht, M.-H. Phan, and H. Srikanth, *Scaling of the Thermally Induced Sign Inversion of Longitudinal Spin Seebeck Effect in a Compensated Ferrimagnet: Role of Magnetic Anisotropy*, Adv. Funct. Mater. 2109170 (2021).

[4] K. Uchida, J. Xiao, H. Adachi, J. Ohe, S. Takahashi, J. Ieda, T. Ota, Y. Kajiwara, H. Umezawa, and H. Kawai, *Spin Seebeck Insulator*, Nat. Mater. **9**, 894 (2010).

[5] Y. Pu, D. Chiba, F. Matsukura, H. Ohno, and J. Shi, *Mott Relation for Anomalous Hall and Nernst Effects in Ga 1- x Mn x As Ferromagnetic Semiconductors*, Phys. Rev. Lett. **101**, 117208 (2008).

[6] R. Nagasawa, K. Oyanagi, T. Hirai, R. Modak, S. Kobayashi, and K. Uchida, *Anomalous Ettingshausen Effect in Iron--Carbon Alloys*, Appl. Phys. Lett. **121**, 62401 (2022).

[7] M. Ikhlas, T. Tomita, T. Koretsune, M.-T. Suzuki, D. Nishio-Hamane, R. Arita, Y. Otani, and S. Nakatsuji, *Large Anomalous Nernst Effect at Room Temperature in a Chiral Antiferromagnet*, Nat. Phys. **13**, 1085 (2017).

[8] A. Sakai, Y. P. Mizuta, A. A. Nugroho, R. Sihombing, T. Koretsune, M.-T. Suzuki, N. Takemori, R. Ishii, D. N. -Hamane, R. Arita *et al.*, *Giant Anomalous Nernst Effect and Quantum-Critical Scaling in a Ferromagnetic Semimetal*, Nat. Phys. **14**, 1119 (2018).

[9] S. N. Guin, K. Manna, J. Noky, S. J. Watzman, C. Fu, N. Kumar, W. Schnelle, C. Shekhar, Y. Sun, J. Gooth *et al.*, *Anomalous Nernst Effect beyond the Magnetization*

Scaling Relation in the Ferromagnetic Heusler Compound Co2MnGa, NPG Asia Mater. **11**, 16 (2019).

[10] H. Yang, W. You, J. Wang, J. Huang, C. Xi, X. Xu, C. Cao, M. Tian, Z.-A. Xu, J. Dai *et al.*, *Giant Anomalous Nernst Effect in the Magnetic Weyl Semimetal Co 3 Sn 2 S 2*, Phys. Rev. Mater. **4**, 24202 (2020).

[11] L. Ding, J. Koo, L. Xu, X. Li, X. Lu, L. Zhao, Q. Wang, Q. Yin, H. Lei, B. Yan *et al.*, *Intrinsic Anomalous Nernst Effect Amplified by Disorder in a Half-Metallic Semimetal*, Phys. Rev. X **9**, 41061 (2019).

[12] A. Sakai, S. Minami, T. Koretsune, T. Chen, T. Higo, Y. Wang, T. Nomoto, M. Hirayama, S. Miwa, D. N. -Hamane *et al.*, *Iron-Based Binary Ferromagnets for Transverse Thermoelectric Conversion*, Nature **581**, 53 (2020).

[13] T. Chen, S. Minami, A. Sakai, Y. Wang, Z. Feng, T. Nomoto, M. Hirayama, R. Ishii, T. Koretsune, R. Arita *et al.*, *Large Anomalous Nernst Effect and Nodal Plane in an Iron-Based Kagome Ferromagnet*, Sci. Adv. **8**, eabk1480 (2022).

[14] T. Asaba, V. Ivanov, S. M. Thomas, S. Y. Savrasov, J. D. Thompson, E. D. Bauer, and F. Ronning, *Colossal Anomalous Nernst Effect in a Correlated Noncentrosymmetric Kagome Ferromagnet*, Sci. Adv. **7**, eabf1467 (2021).

[15] Y. Pan, C. Le, B. He, S. J. Watzman, M. Yao, J. Gooth, J. P. Heremans, Y. Sun, and C. Felser, *Giant Anomalous Nernst Signal in the Antiferromagnet YbMnBi2*, Nat. Mater. **21**, 203 (2022).

[16] Y. Sakuraba, K. Hyodo, A. Sakuma, and S. Mitani, *Giant Anomalous Nernst Effect in the C o 2 MnA l 1- x S i x Heusler Alloy Induced by Fermi Level Tuning and Atomic Ordering*, Phys. Rev. B **101**, 134407 (2020).

[17] A. Chanda, D. Rani, J. Nag, A. Alam, K. G. Suresh, M. H. Phan, and H. Srikanth, *Emergence of Asymmetric Skew-Scattering Dominated Anomalous Nernst Effect in the*

Spin Gapless Semiconductors Co 1+ x Fe 1- x CrGa, Phys. Rev. B **106**, 134416 (2022).

[18] A. Ghosh, A. De, and S. Nair, *Large Anomalous Nernst Effect across the Magneto-Structural Transition in a Bulk Ni-Co-Mn-Sn Full Heusler Alloy*, Appl. Phys. Lett. **113**, 262405 (2018).

[19] A. De, A. K. Singh, S. Singh, and S. Nair, *Temperature Dependence of the Anomalous Nernst Effect in Ni 2 Mn Ga Shape Memory Alloy*, Phys. Rev. B **103**, L020404 (2021).

[20] J. Nag, D. Rani, D. Singh, R. Venkatesh, B. Sahni, A. K. Yadav, S. N. Jha, D. Bhattacharyya, P. D. Babu, K. G. Suresh *et al.*, *CoFeVSb: A Promising Candidate for Spin Valve and Thermoelectric Applications*, Phys. Rev. B **105**, 144409 (2022).

[21] See Supplemental Material at for additonal data, which includes the experimental details related to the ANE measurements, computational details, magnetic properties of CoFeVSb sample and theoretically estimated thermopower vs. chemical potential at various temperatures. See also references [17, 20, 22–29, 30–37] therein.

[22] J. M. Ziman, *Principles of the Theory of Solids* (Cambridge university press, 1972).

[23] S. Chatterjee, S. Chatterjee, S. Giri, and S. Majumdar, *Transport Properties of Heusler Compounds and Alloys*, J. Phys. Condens. Matter (2021).

[24] D. Bombor, C. G. F. Blum, O. Volkonskiy, S. Rodan, S. Wurmehl, C. Hess, and B. Büchner, *Half-Metallic Ferromagnetism with Unexpectedly Small Spin Splitting in the Heusler Compound Co 2 FeSi*, Phys. Rev. Lett. **110**, 66601 (2013).

[25] A. Barry, J. M. D. Coey, L. Ranno, and K. Ounadjela, *Evidence for a Gap in the Excitation Spectrum of CrO 2*, J. Appl. Phys. **83**, 7166 (1998).

[26] A. W. Forbes, R. P. Dulal, N. Bhattarai, I. L. Pegg, and J. Philip, *Experimental Realization and Magnetotransport Properties of Half-Metallic Fe 2 Si*, J. Appl. Phys. **125**, 243902 (2019).

[27] P. A. Lee and T. V Ramakrishnan, *Disordered Electronic Systems*, Rev. Mod. Phys. **57**, 287 (1985).

[28] J. P. Heremans, V. Jovovic, E. S. Toberer, A. Saramat, K. Kurosaki, A. Charoenphakdee, S. Yamanaka, and G. J. Snyder, *Enhancement of Thermoelectric Efficiency in PbTe by Distortion of the Electronic Density of States*, Science (80-.). **321**, 554 (2008).

[29] T. M. Tritt, *Thermoelectric Phenomena, Materials, and Applications*, Annu. Rev. Mater. Res. **41**, 433 (2011).

[30] H.-S. Kim, Z. M. Gibbs, Y. Tang, H. Wang, and G. J. Snyder, *Characterization of Lorenz Number with Seebeck Coefficient Measurement*, APL Mater. **3**, 41506 (2015).

[31] J. Callaway, *Low-Temperature Lattice Thermal Conductivity*, Phys. Rev. **122**, 787 (1961).

[32] J. Callaway, *Model for Lattice Thermal Conductivity at Low Temperatures*, Phys. Rev. **113**, 1046 (1959).

[33] F. J. DiSalvo, *Thermoelectric Cooling and Power Generation*, Science (80-.). **285**, 703 (1999).

[34] R. Ramos, M. H. Aguirre, A. Anadón, J. Blasco, I. Lucas, K. Uchida, P. A. Algarabel, L. Morellón, E. Saitoh, and M. R. Ibarra, *Anomalous Nernst Effect of Fe 3 O 4 Single Crystal*, Phys. Rev. B **90**, 54422 (2014).

[35] P. Jiménez-Cavero, I. Lucas, D. Bugallo, C. López-Bueno, R. Ramos, P. A. Algarabel, M. R. Ibarra, F. Rivadulla, and L. Morellón, *Quantification of the Interfacial and Bulk Contributions to the Longitudinal Spin Seebeck Effect*, Appl. Phys. Lett. **118**, 92404 (2021).

[36] A. De, A. Ghosh, R. Mandal, S. Ogale, and S. Nair, *Temperature Dependence of the Spin Seebeck Effect in a Mixed Valent Manganite*, Phys. Rev. Lett. **124**, 17203 (2020).

[37] T. Ashworth, J. E. Loomer, and M. M. Kreitman, *Thermal Conductivity of Nylons and Apiezon Greases*, in *Advances in Cryogenic Engineering* (Springer, 1973), pp. 271–279.

[38] A. Ghosh, A. Chanda, and R. Mahendiran, *Anomalous Nernst Effect in Pr0. 5Sr0. 5CoO3*, AIP Adv. **11**, 35031 (2021).

[39] D. Kan and Y. Shimakawa, *Strain Effect on Thermoelectric Properties of SrRuO3 Epitaxial Thin Films*, Appl. Phys. Lett. **115**, 22403 (2019).

[40] J. Xu, W. A. Phelan, and C.-L. Chien, *Large Anomalous Nernst Effect in a van Der Waals Ferromagnet Fe3GeTe2*, Nano Lett. **19**, 8250 (2019).

[41] N. F. Mott, H. Jones, H. Jones, and H. Jones, *The Theory of the Properties of Metals and Alloys* (Courier Dover Publications, 1958).

[42] N. Nagaosa, J. Sinova, S. Onoda, A. H. MacDonald, and N. P. Ong, *Anomalous Hall Effect*, Rev. Mod. Phys. **82**, 1539 (2010).

[43] X. Li, L. Xu, L. Ding, J. Wang, M. Shen, X. Lu, Z. Zhu, and K. Behnia, *Anomalous Nernst and Righi-Leduc Effects in Mn 3 Sn: Berry Curvature and Entropy Flow*, Phys. Rev. Lett. **119**, 56601 (2017).

[44] L. Xu, X. Li, L. Ding, T. Chen, A. Sakai, B. Fauqué, S. Nakatsuji, Z. Zhu, and K. Behnia, *Anomalous Transverse Response of Co 2 MnGa and Universality of the Room-Temperature \$α\$ i j A/\$σ\$ i j A Ratio across Topological Magnets*, Phys. Rev. B **101**, 180404 (2020).

[45] K. Behnia and H. Aubin, *Nernst Effect in Metals and Superconductors: A Review of Concepts and Experiments*, Reports Prog. Phys. **79**, 46502 (2016).

[46] K. Behnia, *The Nernst Effect and the Boundaries of the Fermi Liquid Picture*, J. Phys. Condens. Matter **21**, 113101 (2009).

[47] N. Marzari and D. Vanderbilt, *Maximally Localized Generalized Wannier Functions*

for Composite Energy Bands, Phys. Rev. B **56**, 12847 (1997).

[48] I. Souza, N. Marzari, and D. Vanderbilt, *Maximally Localized Wannier Functions for Entangled Energy Bands*, Phys. Rev. B **65**, 35109 (2001).

[49] N. Marzari, A. A. Mostofi, J. R. Yates, I. Souza, and D. Vanderbilt, *Maximally Localized Wannier Functions: Theory and Applications*, Rev. Mod. Phys. **84**, 1419 (2012).

[50] I. Galanakis, P. H. Dederichs, and N. Papanikolaou, *Slater-Pauling Behavior and Origin of the Half-Metallicity of the Full-Heusler Alloys*, Phys. Rev. B **66**, 174429 (2002).

[51] J. L. Cohn, J. J. Neumeier, C. P. Popoviciu, K. J. McClellan, and T. Leventouri, *Local Lattice Distortions and Thermal Transport in Perovskite Manganites*, Phys. Rev. B **56**, R8495 (1997).

[52] S. Bhattacharya, A. Mehdizadeh Dehkordi, S. Tennakoon, R. Adebisi, J. R. Gladden, T. Darroudi, H. N. Alshareef, and T. M. Tritt, *Role of Phonon Scattering by Elastic Strain Field in Thermoelectric Sr1- XYxTiO3- $δ$*, J. Appl. Phys. **115**, 223712 (2014).

[53] P. G. Klemens, *Thermal Resistance Due to Point Defects at High Temperatures*, Phys. Rev. **119**, 507 (1960).

[54] G. A. Slack and S. Galginaitis, *Thermal Conductivity and Phonon Scattering by Magnetic Impurities in CdTe*, Phys. Rev. **133**, A253 (1964).

[55] J. Yang, D. T. Morelli, G. P. Meisner, W. Chen, J. S. Dyck, and C. Uher, *Influence of Electron-Phonon Interaction on the Lattice Thermal Conductivity of Co 1- x Ni x Sb 3*, Phys. Rev. B **65**, 94115 (2002).

[56] C. Fu, H. Xie, T. J. Zhu, J. Xie, and X. B. Zhao, *Enhanced Phonon Scattering by Mass and Strain Field Fluctuations in Nb Substituted FeVSb Half-Heusler Thermoelectric Materials*, J. Appl. Phys. **112**, 124915 (2012).

[57] T. J. Zhu, C. G. Fu, H. H. Xie, Y. T. Liu, B. Feng, J. Xie, and X. B. Zhao, *Lattice Thermal Conductivity and Spectral Phonon Scattering in FeVSb-Based Half-Heusler Compounds*, EPL (Europhysics Lett. **104**, 46003 (2013).

[58] *Http://Www.Wannier.Org/*, (unpublished).